Mid-infrared hollow core fiber drawn from a 3D printed chalcogenide glass preform

Julie Carcreff, François Cheviré, Elodie Galdo, Ronan Lebullenger, Antoine Gautier, Jean-Luc Adam, David Le Coq, Laurent Brilland, Radwan Chahal, Gilles Renversez, et al.

Mid-infrared hollow core fiber drawn from a 3D printed chalcogenide glass preform

JULIE CARCREFF,[1] FRANCOIS CHEVIRE,[1] ELODIE GALDO,[1] RONAN LEBULLENGER,[1] ANTOINE GAUTIER,[1] JEAN LUC ADAM,[1] DAVID LE COQ,[1] LAURENT BRILLAND,[2] RADWAN CHAHAL,[2] GILLES RENVERSEZ, [3] AND JOHANN TROLES[1,*]

[1]*Université Rennes, CNRS, ISCR-UMR 6226, F-35000 Rennes, France*
[2]*SelenOptics, 263 Avenue Gal Leclerc, 35042 Rennes, France*
[3]*Aix-Marseille Université, CNRS, Centrale Marseille, Institut Fresnel, 13013 Marseille, France*
**johann.troles@univ-rennes1.fr*

Abstract: We report the fabrication of a microstructured optical fiber drawn from a soft glass 3D printed preform. For this proof of concept, a chalcogenide glass that is well known for its capability to be shaped at low temperature and its mid-infrared transmission was selected: $Te_{20}As_{30}Se_{50}$. The obtained negative curvature hollow core fiber shows several transmission bands in the 2-12 μm range that are reproduced numerically using finite element-based simulations and coupled mode theory.

1. Introduction

Additive manufacturing, or 3D printing has proven to be a powerful elaboration method in materials science. Predominantly used for polymers [1-3] additive manufacturing has been extended to metals [4], to ceramics [5], and quite recently to glasses [6-12]. In this study, the fabrication of a chalcogenide microstructured optical fiber (MOF) drawn from a 3D printed preform is reported for the first time. Transmission of infrared light through the fiber core is demonstrated, and the recorded main optical transmission bands of the as-prepared fiber are successfully compared to simulated ones. For this proof of concept, a soft glass such as chalcogenide glass has been chosen because of its well-known capability to be shaped at low temperature (T<600 °C) and its mid-IR transparency. Chalcogenide glass fibers have been implemented with success in innovative mid-IR systems for versatile mid-IR fiber transmission [13,14], supercontinuum generation [15-18], and sensing [19]. The objective of this work is to realize a chalcogenide hollow core (HC) MOF for transmission in the mid-IR region (2-12 μm) [20,21], by using an original additive manufacturing process. Actually, with HC MOF structure, it is possible to obtain transmission beyond the transmission limits of a solid core fiber and very low attenuation [22]. Laser power delivery would be greatly improved by using such fibers as compared to solid core fibers. It would then be possible to propagate a laser beam in the infrared, like CO_2 laser at 10.6 μm, for industrial cutting or for surgery. In this context the $Te_{20}As_{30}Se_{50}$ (TAS) chalcogenide glass showing good mid-IR transmission and a low glass transition temperature (T_g) suitable for 3D printing by thermal filamentation has been chosen. The glass transition temperature of TAS glass is 137°C. Thanks to this low T_g, a viscosity of 10^3-10^2 Pa.s is obtained around 280°C, which is perfectly well adapted for fused filamentation fabrication (FFF) [23]. Such additive manufacturing approach allows the fabrication of preforms with complex designs in a single step within a couple of hours, with a high degree of repeatability and accuracy of the geometry. One can note that the classical way for making MOF preforms is the stack and draw technique [24], which is a time-consuming method and presents limited possible geometries. One can note, that for soft glasses like chalcogenide glasses preform extrusion is also an alternative method to the stack and draw technique [20]. The 3D printing way for obtaining optical fibers is

utilized currently with polymers for which various geometries have been obtained including MOF geometries. In addition, it has been shown that a silica fiber can be drawn from 3D printed preforms made by stereolithography with UV-curable composite resin containing silica particles [11]. However, no MOF obtained from a 3D-printed inorganic glass preform, including chalcogenide glass, has ever been reported. The closest related work deals with the demonstration of 3D printed bulk As_2S_3 glass obtained by FFF [12].

In this paper, a commercial 3D printer, commonly used with plastic filaments, is modified to accept chalcogenide glass rods for the purpose of building structured fiber optic preforms. Chalcogenide glasses are fabricated using methods described elsewhere [25,26] in order to produce suitable feedstocks. A solid glass cylindrical preform was first produced as a vehicle to optimize the 3D printing technique and then drawn into a single-index fiber. This allowed to identify optical losses introduced by the 3D printing technique in excess of those from traditional fiber drawn from solid melt-cast preforms. The technique is then validated by printing a structured preform and drawing that into a hollow-core micro-structured optical fiber (HC-MOF). Fiber transmission was measured in the mid-IR and the resulting optical performance was then simulated using the finite element method (FEM).

2. 3D printed chalcogenide glasses

2.1 Chalcogenide glass synthesis

For the additive manufacturing study, the TAS chalcogenide glass is prepared by the conventional melt-quenching method by, first, introducing high purity As (99.999%), Se (99.999%) and Te (99.999%) in a silica ampoule (12 mm inner diameter), which is then pumped under vacuum for 3 h. Further, the silica ampoule is sealed and placed in a rocking furnace at 850° C during 10 hours to homogenize the melt. The glass is then quenched by immersion of the ampoule in water, and annealed above T_g to remove mechanical constraints. For obtaining the rods used as raw materials for the 3D printer, the 12-mm diameter rods were stretched into 3-mm canes within the drawing tower.

For obtaining a higher optical quality glass, the addition of $TeCl_4$ and aluminum (1000 weight ppm and 100 weight ppm, respectively) to the raw starting elements permits the capture at high temperature of remaining hydrogen, carbon and oxygen by forming HCl, CCl_4, Al_2O_3. The mixture is then cooled down to 700 °C, quenched into water by immersion of the ampoule, and annealed above the glass transition temperature T_g. Then, the chalcogenide glass rod, obtained after opening the ampoule, is placed into a distillation ampoule to be purified by several distillation steps. It is first distilled under dynamic vacuum to eliminate the low vapor pressure impurities such as carbon tetrachloride and HCl residues. In the second step, a distillation under static vacuum permits the elimination of refractory impurities, such as carbon, silica, alumina and other refractory oxides. When the distillation process is complete, the glass is further homogenized at 850 °C for 10 hours, cooled to 550 °C, quenched in water, and annealed slightly above T_g. This purified glass rod is used for drawing a single-index fiber whose optical attenuation serves as a reference for the results obtained with fibers drawn from 3D-printed preforms.

2.2 3D printing process

The 3D-printing set-up is based on a customized commercial cartesian Arduino-based RepRap-style 3D printer upgraded for soft glasses and running Marlin firmware [27]. Especially, the feeding mechanism is customized to handle suitably brittle materials. This mechanism is supplied with 500 mm long glass rods of 3 mm diameters that are produced by the fiber drawing method. An extruder drives the raw material filament to a nozzle heated well above T_g. The printer head moves along the X and Z axes while depositing the TAS glass as 100-µm thick layers and the bed plate moves along the Y axis. The temperature of the extruder head was fixed at 300 °C. The size of the nozzle, and consequently, the width of

the printed filament was about 400 µm. The TAS glass was deposited on a sodalime silicate glass bed plate heated around 140 °C (i.e. slightly above T_g) in order to ensure a good adherence of the first printed layers. For optimum control of the extrusion and the nozzle displacement during printing, a simple G-code input file was written using circular motion commands. Let us note that for those proof-of-concept experiments, the 3D printing process is not yet done under controlled atmosphere but in ambient conditions. The 3D printer is installed under a fume hood in order to protect the room environment from any volatile gases that could be generated during printing. Figure 1 shows an example of a 3D-printed chalcogenide TAS glass cylinder (preform used for drawing the single index "printed" fiber, see Section 3.1) and an inner part of it (obtained by cleaving the cylinder), observed by an optical microscope and (inset) a scanning electron microscope. No interface is visible between the filaments in the XY-plane or layers along the z-axis of deposited glass, indicating a good intrinsic quality of the printing. However, several bubbles are observed due to imperfect filaments collapsing and/or gas bubbles formed by the degassing of volatile compounds such as arsenic oxides or selenide oxides [26].

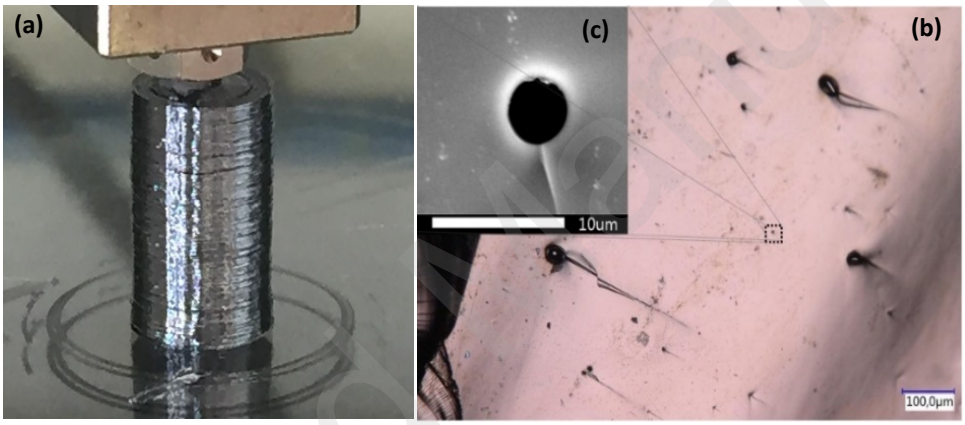

Fig. 1. Bulk 3D printed Chalcogenide glass: (a) 8 mm diameter printed chalcogenide TAS glass cylinder (during the printing), (b) Inner part of the glass cylinder observed by an optical microscope and (c) by scanning electron microscope.

The physical properties of the printed glass have been compared to the ones of the initial glass and reported in Table 1. Energy dispersive spectroscopy (EDS) and differential scanning calorimetry (DSC) measurements confirm that the composition and the glass transition temperature have not been altered during the printing process. Small bubbles present in the glass account for the lower density and result in an increased light scattering that can explain the higher optical losses, from 8 to 28 dB/m in the mid-IR (Table 1).

Table 1. Physical properties of as-prepared and printed $Te_{20}As_{30}Se_{50}$

	Composition* (± 1 %)	T_g (°C) (± 2 °C)	Fiber transmission range (µm)	Density (g/cm^3, ± 1 %)	Attenuation at 7 µm** (dB/m, ± 5%)
Initial	$Te_{20}As_{30}Se_{50}$	137	2-12	4.86	8
Printed glass	$Te_{21}As_{29}Se_{50}$	136	2-12	4.63	28

*From EDS analysis, **more details Section 3.1

2.3 Hollow core 3D printed preform

The selected geometry for investigating the realization of 3D printed preform is a simple 6-capillary ring of an anti-resonant structure [28-30] as shown in Fig. 2. After 4 hours of printing, a 30-mm long hollow-core chalcogenide preform has been obtained. The outer diameter is 16 mm, the inner diameter 12 mm, and the 6 capillaries show a diameter of 3.4 mm with a thickness close to 0.4 mm (Fig. 2), which is actually the size of a single trace of the printing nozzle. Let us note that the cladding is made from 5 traces.

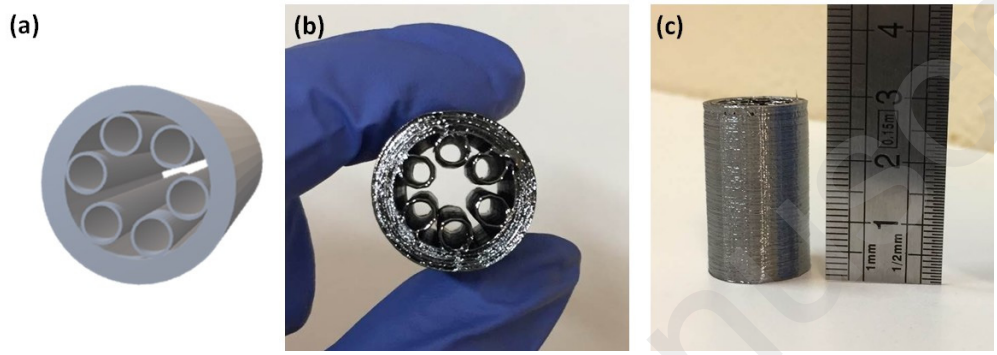

Fig. 2. The printed preform: (a) computed view of the targeted design, loaded on the software of the customized 3D printer, (b) cross-section view of the chalcogenide printed preform, (c) side view of the printed preform with a centimeter scale

Table 2. Geometrical parameters of the printed preform and the obtained fiber

	Clad (µm, ± 1 %)			Capillaries (µm, ± 1 %)			Core size (µm, ± 1%)
	Outer ⌀	Inner ⌀	Inner/outer ratio	Outer ⌀	Inner ⌀	Inner/outer ratio	
Printed preform	16000	11800	0.74	3400	2600	0.76	5050
Fiber from printed preform	412	322	0.78	66	40	0.61	217

2.4 Drawing process

The printed preform was used to manufacture an anti-resonant hollow-core fiber by using a homemade drawing tower specifically designed for low- T_g glasses. The preform is placed in a narrow drawing furnace that can permit to draw short preforms. When the furnace reaches the drawing temperature around 270 °C, a glass drop appears and falls down under gravity forming a glass fiber which is then reeled on a spool in rotary motion. At the same time, the preform is moved down, feeding the drawing furnace. For a given feeding speed of the preform, the diameter of the fiber is controlled by the spool speed. A helium gas flow of 2.5 L/min provides an inert atmosphere around the preform. Usually, during the drawing of MOFs, a differential pressure is applied in the core and in the different capillaries in order to control the geometry. However, for this proof of concept study, no differential pressure was applied. Consequently, the geometry of the capillaries has changed during drawing due to surface tension, more particularly the ratio between the inner and the outer diameter (Table 2). Nevertheless, it has been demonstrated that a preform obtained by additive manufacturing can be drawn into a fiber in which the initial shape is globally maintained (see Fig. 3). The final parameters of the fiber are summarized in Table 2. Although the printed hollow core preform is only 3 cm long, several meters of fibers have been obtained.

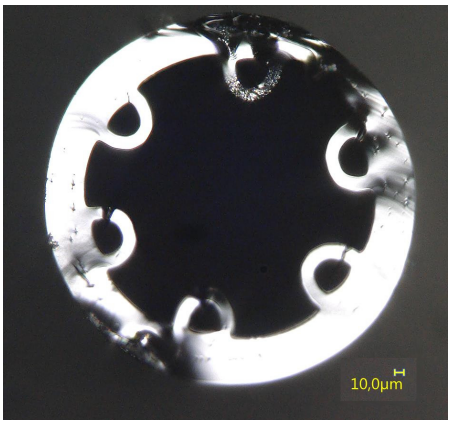

Fig. 3. "Printed" hollow core fiber cross-section.

3. Mid-IR optical measurements

Attenuation of optical fibers were measured by means of a Fourier-transform infrared (FTIR) spectrometer (Bruker, Vector 22) equipped with a mercury-cadmium-tellurium (MCT) detector. Four types of fibers have been analyzed: a single-index fiber made from purified glass, a single-index fiber made from unpurified glass, a single-index fiber made from printed unpurified glass, and a hollow-core fiber made from printed unpurified glass.

3.1 Bulk single-index fibers

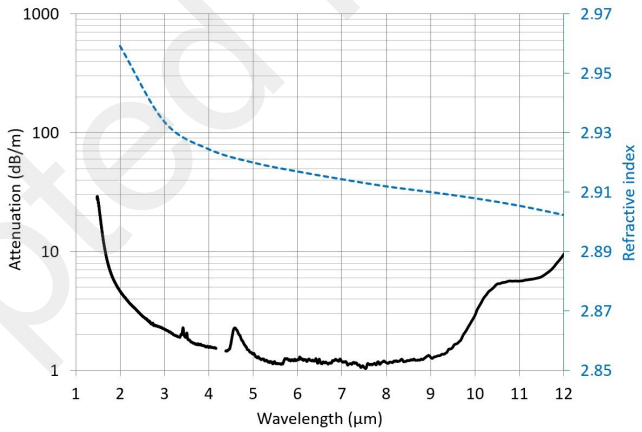

Fig. 4. Optical properties of the $Te_{20}As_{30}Se_{50}$ chalcogenide glass fiber in the mid-IR region. Single index optical fiber attenuation: black solid line with the left vertical scale, refractive index: blue dashed line with the right vertical scale.

The intrinsic mid-IR window of the TAS glass fiber was determined by measuring the attenuation of a single-index fiber made from purified glass (see Fig. 4). The measurement was realized by the classical cut-back method applied to a fiber of 12-meter initial length. The attenuation curve in Fig. 4 corresponds to the average of 3 measurements, the final length of the fiber being equal to 1 meter. Considering that the transparency limit corresponds to a 10 dB/m absorption, one can conclude that a TAS fiber made of purified glass transmits light

between 2 and 12 µm, with a minimum attenuation of 1 dB/m at 7.5 µm. The peak at 4.55 µm is due to Se-H absorption, which results from a contamination by residual hydrogen adsorbed on the silica ampoules utilized for TAS glass synthesis [25,26].

Complementary measurements were carried out to better understand the effects of 3D printing on the glass optical properties. In this study, where the objective is to demonstrate the concept of making microstructured optical fibers from a printed preform, unpurified TAS glasses were implemented. The preparation of unpurified glasses is more straightforward than that of purified ones. Attenuation curves were obtained by using the cut-back method on 1-meter long fibers drawn from the initial glass preform, made from the same raw glass composition as the one used for feeding the 3D printer, and from a printed glass cylinder (8 mm diameter). Results are shown in Fig. 5. Comparison of Figs. 4 and 5 indicates that single-index fibers possess the same overall Mid-IR transparency window, from 2 to 10 µm, whether the glass is initially purified or not. However, the minimum loss is significantly higher in the unpurified fiber with a value of nearly 8 dB/m at 7.5 µm. Also, two intense absorption peaks at 2.9 µm and 6.3 µm due to, respectively, OH chemicals bonds and molecular H_2O chemicals bonds were observed. OH and H_2O are classical pollutants in unpurified chalcogenide glasses [25]. Compared to these two intense absorptions, the Se-H peak at 4.55 µm is too weak to be observed in Fig. 5. Above 10 µm, the apparent decrease of attenuation is an artefact due to degraded signal intensity at the output of the fiber. The single-index fiber obtained from a printed glass shows an important increase of the optical losses, which reach 28 dB/m at 7.5 µm. This important increase can be explained by two main reasons: the presence of scattering bubbles (already observed in a bulk 3D printed TAS glass, Fig. 1) and some weak crystallization of the glass occurring during printing, which is done under ambient air for those proof of concept experiments. Moreover, in addition to the OH and molecular H_2O signatures at 2.9 µm and 6.3 µm, numerous other IR absorption peaks are observed. The peak at 3.3 µm is due to C-H chemical bonds induced by an organic pollution, while Se-H bonds are responsible for the absorption at 4.55 µm. Carbon impurities, which are not present in fibers prepared by the classical method, are likely to originate from traces of hydrocarbons present in the 3D printer. The reappearance of hydrogen results from a chemical reaction between the glass and moisture in ambient atmosphere, during printing. The origin of bands at 5.8 µm, 6.8 µm, and 7.2 µm could not be established. Finally, the 7.9 µm and 9.1 µm absorption peaks could be attributed to metal-oxygen vibrations due to a weak oxidation of the chalcogenide glass during printing.

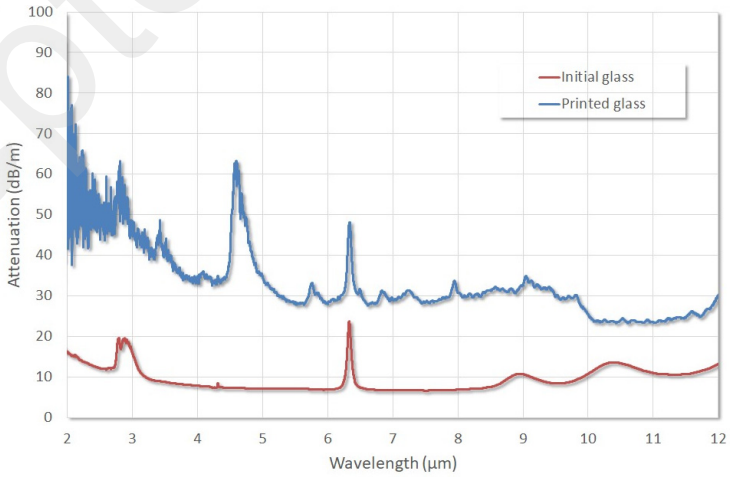

Fig. 5. Attenuation spectra of the initial glass fiber (red curve) and the printed glass fiber (blue curve).

3.2 Printed hollow core fiber

The high optical losses of the fiber (probably close to 100 dB/m, see modeling part Section4) did not permit to achieve any cut back measurement and attenuation measurement. However, light transmission of a 20-cm long hollow-core fiber drawn from the printed preform has been obtained and investigated (Fig. 6). The transmission curve was also obtained by using the FTIR spectrometer mentioned above (Fig. 6(a)). The Mid-IR light coming from the black body source of the FTIR was injected into the 20-cm long fiber. Due to the large size of the spot light (> 1mm^2), part of the light was injected not only in the core but also in the clad of the hollow-core fiber. To make sure that the transmission curve corresponds to the true transmission through the hollow core of the fiber, an absorbing coating (Ga-Sn alloy) was deposited on the surface of the fiber. Indeed, this coating permits to suppress all the cladding modes. Near-field measurements were carried out with an infrared camera working in the 7-13 µm wavelength range (FLIR A655sc). Figure 6(b) shows the profile of the light beam at the output of the fiber, recorded with an infrared camera and it clearly demonstrates that the mid-IR light propagates in the hollow core of the MOF. The Mid-IR light spectrum propagating in the core of the fiber was recorded by using the MCT detector of the FTIR. The result is reported in Fig. 6(a). The numerous transmission bands observed between 2 and 12 µm are characteristic of the propagation behavior of a negative curvature fiber (see Ref. [29] and references therein for a comprehensive review).

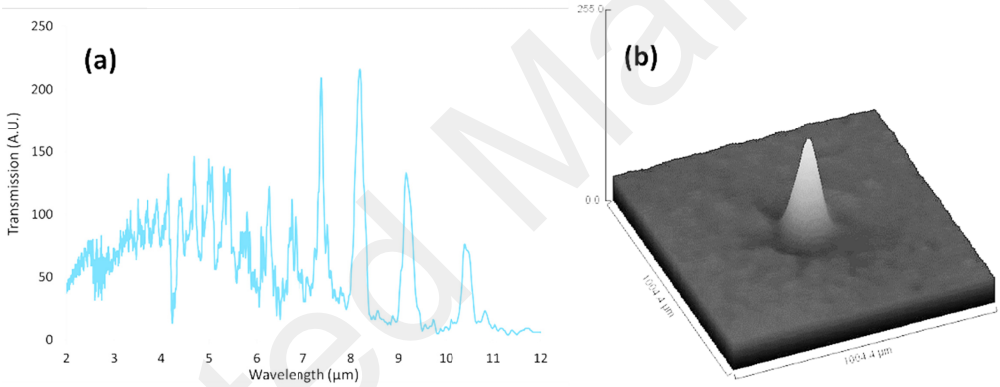

Fig. 6. Mid-infrared transmission spectrum of the hollow core fiber drawn from the 3D printed glass preform: (a) Transmission spectrum of a 20 cm-long "printed" fiber, (b) 3D Mid-IR output profile recorder with a microbolometer camera in the [7-13 µm] range.

4. Modeling and comparison with experimental results

The guiding properties of the HC-MOF covered by the absorbing layer were analyzed using a homemade mode solver based on the finite element method [31,32] and coupled mode theory. The simulations were performed from the HC-MOF cross-section of the tested fiber recorded experimentally and the TAS material dispersion and losses (Figs. 4 and 5). Assuming that the fiber cross-section is invariant along the propagation axis we can define a simple modal problem [33]. This eigenvalue problem is solved numerically using the finite element method (FEM) [34]. We use a vector FEM based on the Galerkin approach that provides the propagation constants (eigenvalues) and the associated mode profiles (eigenvectors). We use the gmsh/getdp free open-source softwares [35,36]. Our FEM approach is described in details in Ref. [31]. It has already been used successfully for many kinds of microstructured optical fibers including ones where the fiber profiles were obtained from scanning electron microscopy images [37,38]. It is worth mentioning that the surface roughness of the interfaces

of the 3D printed fiber that can generate losses in this hollow core fiber [39,40] has not been taken into account in the simulations. The reasons are that it has not been characterized yet and the high level of the computed propagating losses suggests that the losses induced by the surface roughness do not represent the key factor. Furthermore, these losses cannot explain the observed band structure in the recorded transmission spectrum.

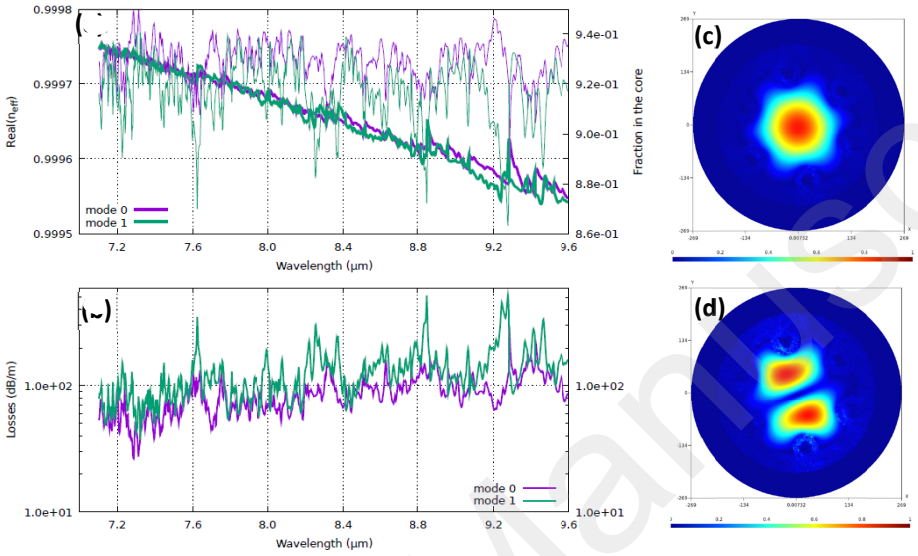

Fig. 7. Simulation results in the wavelength range [7.1-9.6] µm. (a) Real parts (thick curves) and fraction of the electric field modulus in the core (thin curves) for the two main core-localized modes. (b) Losses for the two main core-localized modes. (c and d) mode profiles at 9.2 µm (modulus of electric fields) for the two main core localized modes

As depicted in Fig. 7(a), the dispersion curves of the two main modes (Figs. 7(c) and 7(d)), defined here as the core of these two modes cannot be used to determine the transmission bands observed experimentally (see bottom panel in Fig. 8(d) which is a zoom of Fig. 6(a)). The same conclusion can be drawn for the study of the losses of these two modes as shown in Fig. 7(b). The transmission bands present in Fig. 6(a) or Fig. 8(b) (measured transmission) are not present in the simulated loss spectrum (Fig. 7(b)).In order to explain the existence of the bands, the usual guidance mechanism in such HC-MOF, also called negative curvature MOF, must be considered [29]. In the simplest case, it is well established that when the fiber can be considered as invariant along its axis, the losses of the fundamental mode must be studied as a function of the wavelength, and the low-loss regions are bounded by high loss regions where this core-localized mode couples to some regions of the cladding that are responsible for the loss increase. Usually, the fiber cross-section is optimized in order to ensure the smallest coupling between the main core-localized modes and the glass cladding of the fiber at specific wavelengths. But, in our case, this simple loss analysis is not sufficient to explain the positions of the transmission peaks at least for three reasons: (I) the obtained fiber profile does not reach the initially targeted design, (II) it is not symmetric and consequently the two fundamental modes (associated to two polarization axis) are now quite different from each other, (III) due to the fabrication process the fiber is not fully invariant along its propagation axis. Consequently, coupled mode theory [33,41,42] is necessary to explain the observed phenomenon. In this framework, not only the fundamental mode associated to the cross-section of the fiber with its absorbing coating must be determined but also the higher order modes including the lossy ones that are partially localized in the glass cladding but still couple to the fundamental mode. When these modes are computed, the coupling coefficients

between them and the fundamental mode can be evaluated as well. The loss mechanism of the fundamental mode and therefore its transmission bands can then be explained: if this core-localized mode couples only very weakly to other modes, it will keep on propagating in the fiber core with effective losses only slightly larger than its intrinsic propagating losses. Nevertheless, if the fundamental mode couples directly to other more-lossy modes or to modes that strongly couple to such lossy modes, it will then decay more rapidly, and its transmission will vanish at the end of the 20 cm-long fiber. As explained in references [33,41,42], in the coupled mode theory, the coupling coefficients (longitudinal and transverse ones) between the modes m and n denoted by K_{mn} are the key quantities in this analysis. The formula used to compute the coupling coefficients K_{mn} between a mode m and a mode n are the ones given in [41] with a focus on the dependence in the modal profiles for the electric field and not in the permittivity changes since they are the same for all the modes.

The sum of the modulus of these coefficients K_{0n} describing the coupling between the fundamental mode (m = 0) and the other modes (n) as a function of the wavelength are provided in panel Fig. 7(a).

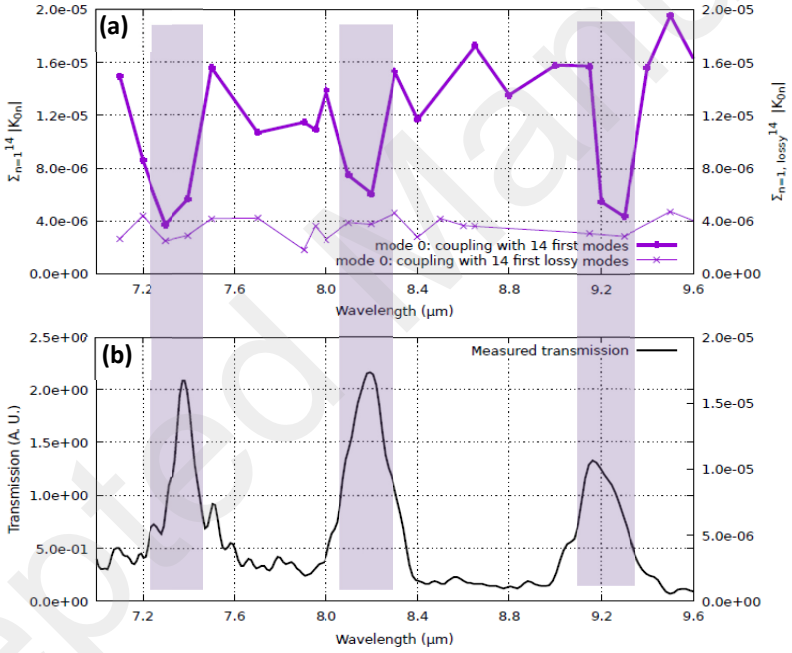

Fig. 8. Simulation results and experimental transmission in the wavelength range [7.1; 9.6] µm. (a) Sum of the coupling coefficients K_{0n} between the fundamental core-localized mode (mode 0) and: with the next 14 higher order core-localized modes (thick curve), and with the first 14 highly lossy modes (thin curve). (b) Zoom of the measured transmission shown in Fig. 6(a) in the studied wavelength range.

Practically, for each studied wavelength, we compute the first 60 modes of the fiber in order to ensure that all the modes of interest are available for the analysis. Then, we compute both the transverse and longitudinal coupling of coefficients between the fundamental mode and the first 14 core localized higher-order modes. Then, we compute the sum of the modulus of these transverse coefficients (thick curve in panel Fig. 8(a)) and the similar sum for the longitudinal coefficients. We also compute the sum of the transverse coefficients and longitudinal ones for the highly lossy modes included in the 60 computed modes such that the

imaginary parts of their effective indices are above 10^{-3} (while the imaginary part of the effective index of the fundamental mode is typically in the [10^{-6}-10^{-5}] range). It is worth to mention that only the results for the transverse coefficient sum for the modes are shown in Fig. 8(a), because like for most fibers, the longitudinal coefficients are typically one order of magnitude smaller than the transverse ones.
As illustrated Figs. 8(a) and 8(b), the transmission peaks correspond to wavelength ranges with a smaller sum of these modulus coefficients between the fundamental core mode and other modes (highlighted spectrum part in Fig. 8) while low transmission regions originate from a large sum of the coupling coefficients to higher-order modes. Since the longitudinal variations of the fiber cross-section are not available, the coupled mode theory-based analysis cannot be taken further. Thus, this limitation can explain the small differences between the central wavelength positions of the computed transmission bands and the measured ones. Nevertheless, the negative curvature fiber guidance mechanism with the localization of its transmission bands is demonstrated.

5. Conclusion

In conclusion, the proof of concept of 3D printing of chalcogenide glass preforms has been demonstrated and such preforms have been drawn into guiding optical fibers (single index fiber and hollow core fiber).
This first ever chalcogenide "printed" hollow core fiber shows significant light transmission bands in the 4-12 µm window. The spectral positions of the most intense bands are confirmed by numerical simulations, considering the recorded fiber cross-section. The important optical losses should strongly be improved by using high optical quality raw glasses, by printing the preforms under controlled atmosphere, and by a better control of the geometrical parameters during fiber drawing. Those results open a new way for the elaboration of chalcogenide and other soft-glass based components such as optical fibers, especially hollow-core MOFs, and also types of other waveguides or lenses.

Funding

This work was funded in part by the European Union through the European Regional Development Fund (ERDF), the Ministry of Higher Education and Research, the French region of Brittany, Rennes Métropole, the French National Research agency and DGA (grant ANR ASTRID DGA FOM-IR-2-20).

References

1. K. Cook, J. Canning, S. Leon-Saval, Z. Reid, M. A. Hossain, J.-E. Comatti, Y. Luo, and G.-D. Peng, "Air-structured optical fiber drawn from a 3D-printed preform," Optics Letters **40**, 3966-3969 (2015).
2. W. Talataisong, R. Ismaeel, T. H. Marques, S. A. Mousavi, M. Beresna, M. Gouveia, S. R. Sandoghchi, T. Lee, C. M. Cordeiro, and G. Brambilla, "Mid-IR Hollow-core microstructured fiber drawn from a 3D printed PETG preform," Scientific reports **8**, 1-8 (2018).
3. Y. Luo, J. Canning, J. Zhang, and G.-D. Peng, "Toward optical fibre fabrication using 3D printing technology," Optical Fiber Technology **58**, 102299 (2020).
4. L. E. Murr, S. M. Gaytan, D. A. Ramirez, E. Martinez, J. Hernandez, K. N. Amato, P. W. Shindo, F. R. Medina, and R. B. Wicker, "Metal Fabrication by Additive Manufacturing Using Laser and Electron Beam Melting Technologies," Journal of Materials Science & Technology **28**, 1-14 (2012).
5. A. Zocca, P. Colombo, C. M. Gomes, and J. Günster, "Additive Manufacturing of Ceramics: Issues, Potentialities, and Opportunities," Journal of the American Ceramic Society **98**, 1983-2001 (2015).
6. G. Marchelli, R. Prabhakar, D. Storti, and M. Ganter, "The guide to glass 3D printing: developments, methods, diagnostics and results," Rapid Prototyping Journal **17**, 187-194 (2011).
7. J. Klein, M. Stern, G. Franchin, M. Kayser, C. Inamura, S. Dave, J. C. Weaver, P. Houk, P. Colombo, M. Yang, and N. Oxman, "Additive Manufacturing of Optically Transparent Glass," 3D Printing and Additive Manufacturing **2**, 92-105 (2015).

8. D. T. Nguyen, C. Meyers, T. D. Yee, N. A. Dudukovic, J. F. Destino, C. Zhu, E. B. Duoss, T. F. Baumann, T. Suratwala, J. E. Smay, and R. Dylla-Spears, "3D-Printed Transparent Glass," Adv. Mater. **29**, 1701181 (2017).
9. F. Kotz, K. Arnold, W. Bauer, D. Schild, N. Keller, K. Sachsenheimer, T. M. Nargang, C. Richter, D. Helmer, and B. E. Rapp, "Three-dimensional printing of transparent fused silica glass," Nature **544**, 337-339 (2017).
10. K. C. Datsiou, E. Saleh, F. Spirrett, R. Goodridge, I. Ashcroft, and D. Eustice, "Additive manufacturing of glass with laser powder bed fusion," Journal of the American Ceramic Society **102**, 4410-4414 (2019).
11. Y. Chu, X. Fu, Y. Luo, J. Canning, Y. Tian, K. Cook, J. Zhang, and G.-D. Peng, "Silica optical fiber drawn from 3D printed preforms," Optics Letters **44**, 5358-5361 (2019).
12. E. Baudet, Y. Ledemi, P. Larochelle, S. Morency, and Y. Messaddeq, "3D-printing of arsenic sulfide chalcogenide glasses," Optical Materials Express **9**, 2307-2317 (2019).
13. B. J. Eggleton, B. Luther-Davies, and K. Richardson, "Chalcogenide photonics," Nat Photon **5**, 141-148 (2011).
14. G. Tao, H. Ebendorff-Heidepriem, A. M. Stolyarov, S. Danto, J. V. Badding, Y. Fink, J. Ballato, and A. F. Abouraddy, "Infrared fibers," Advances in Optics and Photonics **7**, 379-458 (2015).
15. C. R. Petersen, U. Møller, I. Kubat, B. Zhou, S. Dupont, J. Ramsay, T. Benson, S. Sujecki, N. Abdel-Moneim, Z. Tang, D. Furniss, A. Seddon, and O. Bang, "Mid-infrared supercontinuum covering the 1.4–13.3 μm molecular fingerprint region using ultra-high NA chalcogenide step-index fibre," Nature Photonics **8**, 830-834 (2014).
16. S. Venck, F. St-Hilaire, L. Brilland, A. N. Ghosh, R. Chahal, C. Caillaud, M. Meneghetti, J. Troles, F. Joulain, S. Cozic, S. Poulain, G. Huss, M. Rochette, J. M. Dudley, and T. Sylvestre, "2-10 mu m Mid-Infrared Fiber-Based Supercontinuum Laser Source: Experiment and Simulation," Laser & Photonics Reviews **14**(2020).
17. P. Zhang, J. Zhang, P. Yang, S. Dai, X. Wang, and W. Zhang, "Fabrication of chalcogenide glass photonic crystal fibers with mechanical drilling," Optical Fiber Technology **26, Part B**, 176-179 (2015).
18. S. X. Dai, Y. Y. Wang, X. F. Peng, P. Q. Zhang, X. S. Wang, and Y. S. Xu, "A Review of Mid-Infrared Supercontinuum Generation in Chalcogenide Glass Fibers," Applied Sciences-Basel **8**, 28 (2018).
19. P. Toupin, L. Brilland, C. Boussard-Pledel, B. Bureau, D. Mechin, J.-L. Adam, and J. Troles, "Comparison between chalcogenide glass single index and microstructured exposed-core fibers for chemical sensing," Journal of Non-Crystalline Solids **377**, 217-219 (2013).
20. R. R. Gattass, D. Rhonehouse, D. Gibson, C. C. McClain, R. Thapa, V. Q. Nguyen, S. S. Bayya, R. J. Weiblen, C. R. Menyuk, L. B. Shaw, and J. S. Sanghera, "Infrared glass-based negative-curvature anti-resonant fibers fabricated through extrusion," Optics Express **24**, 25697-25703 (2016).
21. C. Wei, R. A. Kuis, F. Chenard, C. R. Menyuk, and J. Hu, "Higher-order mode suppression in chalcogenide negative curvature fibers," Optics Express **23**, 15824-15832 (2015).
22. F. Yu, P. Song, D. Wu, T. Birks, D. Bird, and J. Knight, "Attenuation limit of silica-based hollow-core fiber at mid-IR wavelengths," APL Photonics **4**, 080803 (2019).
23. I. E. Gunduz, M. S. McClain, P. Cattani, G. T. C. Chiu, J. F. Rhoads, and S. F. Son, "3D printing of extremely viscous materials using ultrasonic vibrations," Additive Manufacturing **22**, 98-103 (2018).
24. P. Russell, "Photonic Crystal Fibers," Science **299**, 358 (2003).
25. V. S. Shiryaev, J. L. Adam, X. H. Zhang, C. Boussard-Pledel, J. Lucas, and M. F. Churbanov, "Infrared fibers based on Te-As-Se glass system with low optical losses," Journal of Non-Crystalline Solids **336**, 113-119 (2004).
26. J. Troles, V. Shiryaev, M. Churbanov, P. Houizot, L. Brilland, F. Desevedavy, F. Charpentier, T. Pain, G. Snopatin, and J. L. Adam, "GeSe4 glass fibres with low optical losses in the mid-IR," Optical Materials **32**, 212-215 (2009).
27. https://marlinfw.org.
28. I. A. Bufetov, A. F. Kosolapov, A. D. Pryamikov, A. V. Gladyshev, A. N. Kolyadin, A. A. Krylov, Y. P. Yatsenko, and A. S. Biriukov, "Revolver Hollow Core Optical Fibers," Fibers **6**, 39 (2018).
29. C. Wei, R. Joseph Weiblen, C. R. Menyuk, and J. Hu, "Negative curvature fibers," Advances in Optics and Photonics **9**, 504-561 (2017).
30. J. H. Osório, M. Chafer, B. Debord, F. Giovanardi, M. Cordier, M. Maurel, F. Delahaye, F. Amrani, L. Vincetti, F. Gérôme, and F. Benabid, "Tailoring modal properties of inhibited-coupling guiding fibers by cladding modification," Scientific Reports **9**, 1376 (2019).
31. F. Zolla, G. Renversez, A. Nicolet, B. Kuhlmey, S. Guenneau, D. .Felbacq, A. Argyros, and S. Leon-Saval, eds., *Foundations Of Photonic Crystal Fibres (2nd edition)* (*Imperial College Press, london* 2012).
32. F. Desevedavy, G. Renversez, J. Troles, P. Houizot, L. Brilland, I. Vasilief, Q. Coulombier, N. Traynor, F. Smektala, and J.-L. Adam, "Chalcogenide glass hollow core photonic crystal fibers," Optical Materials **32**, 1532-1539 (2010).
33. A. W. Snyder and J. D. Love, eds., *Optical waveguide theory* (*Chapman & hall, New york*, 1983).
34. J.-M. Jin, *The finite element method in electromagnetics* (John Wiley & Sons, 2015).
35. P. Dular, C. Geuzaine, F. Henrotte, and W. Legros, "A general environment for the treatment of discrete problems and its application to the finite element method," IEEE Transactions on Magnetics **34**, 3395-3398 (1998).

36. C. Geuzaine and J.-F. Remacle, "Gmsh: a three-dimensional finite element mesh generator with built-in pre-and post-processing facilities," in *Proceedings of the Second Workshop on Grid Generation for Numerical Computations, Tetrahedron II*, 2007),
37. M. El-Amraoui, J. Fatome, J. C. Jules, B. Kibler, G. Gadret, C. Fortier, F. Smektala, I. Skripatchev, C. F. Polacchini, Y. Messaddeq, J. Troles, L. Brilland, M. Szpulak, and G. Renversez, "Strong infrared spectral broadening in low-loss As-S chalcogenide suspended core microstructured optical fibers," Opt. Express **18**, 4547-4556 (2010).
38. M. Duhant, W. Renard, G. Canat, T. N. Nguyen, F. Smektala, J. Troles, Q. Coulombier, P. Toupin, L. Brilland, P. Bourdon, and G. Renversez, "Fourth-order cascaded Raman shift in AsSe chalcogenide suspended-core fiber pumped at 2 μm," Opt. Lett. **36**, 2859-2861 (2011).
39. P. Roberts, F. Couny, H. Sabert, B. Mangan, T. Birks, J. Knight, and P. Russell, "Loss in solid-core photonic crystal fibers due to interface roughness scattering," Opt. Express **13**, 7779-7793 (2005).
40. E. N. Fokoua, F. Poletti, and D. J. Richardson, "Analysis of light scattering from surface roughness in hollow-core photonic bandgap fibers," Optics Express **20**, 20980-20991 (2012).
41. H. Kogelnik, "2. Theory of dielectric waveguides," in *Integrated Optics* (Springer Berlin Heidelberg, Berlin, Heidelberg, 1975), pp. 13-81.
42. D. Marcuse, "Theory of dielectric optical waveguides Academic Press," Inc., New York, USA (1991).